



## 2D/2D BiVO<sub>4</sub>/CsPbBr<sub>3</sub> S-scheme heterojunction for photocatalytic CO<sub>2</sub> reduction: Insights into structure regulation and Fermi level modulation

Xiaoyang Yue<sup>a,b</sup>, Lei Cheng<sup>a,b</sup>, Jiajie Fan<sup>c</sup>, Qianjun Xiang<sup>a,b,\*</sup>

<sup>a</sup> State Key Laboratory of Electronic Thin Film and Integrated Devices, School of Electronic Science and Engineering, University of Electronic Science and Technology of China, Chengdu 610054, PR China

<sup>b</sup> Yangtze Delta Region Institute (Huzhou), University of Electronic Science and Technology of China, Huzhou 313001, PR China

<sup>c</sup> School of Materials Science and Engineering, Zhengzhou University, Zhengzhou 450000, PR China

### ARTICLE INFO

#### Keywords:

Steering charge transfer  
Fermi level modulation  
Interfacial interaction regulation  
2D/2D vertical structure  
S-scheme heterojunction

### ABSTRACT

Heterojunction construction is a universal and effective approach to achieve high-efficiency photocatalysts. Towards these well-designed heterojunctions, modulation on steering dynamic charge transfer holds great promise in further performance stimulation. Herein, 2D/2D BiVO<sub>4</sub>/CsPbBr<sub>3</sub> S-scheme heterojunctions, of which CsPbBr<sub>3</sub> nanosheets (NSs) are in-situ face-to-face grown onto BiVO<sub>4</sub> NSs, are designed as cornerstones for further carrier managements. Briefly, with controllable heterostructure regulation, an intimate heterointerface between BiVO<sub>4</sub> and CsPbBr<sub>3</sub> NSs with similar size can be obtained accompanied with a maximally intensified interfacial interaction, largely boosting charge transfer across the interfacial conjunction. Moreover, by further tailoring the intrinsic O vacancy (V<sub>O</sub><sup>••</sup>) of BiVO<sub>4</sub>, the gradient Fermi level shift towards its valence band is finely tuned, yielding an enlarged Fermi level gap and an enhanced internal electric field (IEF) over BiVO<sub>4</sub>/CsPbBr<sub>3</sub> heterojunctions. Such an intensified IEF provides a powerful driving force for directional charge migration, resulting in high charge separation and utilization efficiency. Hence, the optimized BiVO<sub>4</sub>/CsPbBr<sub>3</sub> S-scheme heterojunction features desirable accelerated dynamic carrier mobility, delivering comparably high CO<sub>2</sub>-to-CO conversion with a turnover number (TON) near 230 without any co-catalyst or sacrificial agent. The accelerated S-scheme charge transfer mechanism is revealed in detail by X-ray photoelectron spectroscopy (XPS), theoretical calculations, photo-irradiated Kelvin probe force microscopy and in-situ diffuse reflectance infrared Fourier transform spectroscopy (DRIFTS).

### 1. Introduction

Photocatalytic CO<sub>2</sub> conversion into solar fuels or other value-added chemicals via inexhaustible solar energy poses a promising solution to the imminent energy shortage and rigorous global warming. [1] Restricted by the chemical inertness of CO<sub>2</sub> molecules, sluggish dynamics of the multielectron reactions and high charge recombination rates of photoinduced carriers within semiconductor photocatalysts, considerable design strategies longing for high-efficiency photocatalysts have been exploited, such as single atom design, [2] facet control, [3,4] defect engineering [5,6] and heterojunction construction. [7,8] Despite these great achievements, the low conversion efficiency and poor selectivity for target product are still far from the criterion for practical industrial applications. [9] From the perspective of charge dynamics,

in-depth modulations on further steering charge transfer to achieve a specific migration route, long retained carrier lifetime and high utilization efficiency of photoinduced carriers towards these high-efficiency photocatalysts are highly desirable to achieve further performance stimulation. [10].

Recently developed step-scheme (S-scheme) heterojunctions hold great advantages as the cornerstones for further in-depth modulating charge migration due to their unique internal electric field (IEF) mechanism and the structural diversity. [11–13] Typically, an S-scheme heterojunction contains an oxidation photocatalyst and a reduction photocatalyst with the distinguished work functions and staggered band structure configuration. Theoretically, by enlarging the difference in their work functions or the gap between the Fermi levels, the intensity of the interfacial IEF could be largely enhanced, thus capable of providing

\* Corresponding author at: State Key Laboratory of Electronic Thin Film and Integrated Devices, School of Electronic Science and Engineering, University of Electronic Science and Technology of China, Chengdu 610054, PR China.

E-mail address: [xiangqj@uestc.edu.cn](mailto:xiangqj@uestc.edu.cn) (Q. Xiang).

<https://doi.org/10.1016/j.apcatb.2021.120979>

Received 20 August 2021; Received in revised form 10 November 2021; Accepted 27 November 2021

Available online 4 December 2021

0926-3373/© 2021 Elsevier B.V. All rights reserved.

a much more robust driving force for directional charge migration. [11] Recently, IEF modulations on the heterojunction systems have arisen fast. For example, Tao et al. introduced molybdenum oxide with a large work function to the surface of bismuth tantalum oxyhalide nanosheets, achieving an evidently intensive built-in electric field, of which the properties of interfacial charges can be qualitatively tuned. [14] Li et al. integrated S-scheme and the Schottky junction concurrently on SrTiO<sub>3</sub> to further steer its charge transfer, endowing the as-designed large-scale solar light-driven Ru/SrTiO<sub>3</sub>/TiO<sub>2</sub>/FTO device photocatalyst with dense and stable hydrogen bubbles upon light irradiation. [15] These reports demonstrate the superiority of IEF modulation and provide the feasibility for potential applications on S-scheme heterojunctions. Nevertheless, IEF modulation towards S-scheme photocatalysts is rarely reported.

Monoclinic BiVO<sub>4</sub>, as a typical oxidation photocatalyst, arouses our attention due to its abundant resources, low toxicity and high convenience in structural regulation and defect engineering. [16,17] Tuning the content of the O vacancy in BiVO<sub>4</sub> can inevitably alter the Fermi level because of its positive charged characteristic. [18,19] And by virtue of such merit, the adjustable gap of Fermi levels can be achieved when BiVO<sub>4</sub> is coupled with a suitable reduction photocatalyst. Fortunately, previous studies demonstrated that CsPbBr<sub>3</sub> possesses a more negative conduction band (CB) while broader light-harvesting ability compared with TiO<sub>2</sub>, indicating its huge potential as a reduction photocatalyst in visible light-driven photocatalysis. [20,21] Although BiVO<sub>4</sub> and CsPbBr<sub>3</sub> meet the prerequisites for S-scheme heterojunction construction such as their distinguished work functions and staggered band structure configuration, no prior work has achieved desirable S-scheme heterojunction by coupling these two semiconductor materials, let alone accurate Fermi level modulation to further steer charge migration.

From another perspective on structural diversity of S-scheme heterojunctions, an intimate interface with intensive interfacial interaction is of vital significance for its charge migration, which is highly correlated with their structures. [22,23] Amongst various structures, the 2D/2D structure in heterojunction systems is highly preferred for its superior advantages such as large-area interface contact, rich active sites, and shortened diffusion and transport distance of the photoinduced carriers. [24–26] More importantly, their interfacial interactions can be artificially regulated to various types such as 2D/2D van der Waals heterojunction [27] and Schottky heterojunction [28] depending on their assembly methods, material categories and synthetic conditions. [29–31] Therefore, structural regulation to robust interfacial interaction between two semiconductors will also favourably promote quick charge migration. Inspired by all of these merits and achievements, an S-scheme heterojunction with 2D/2D structure and simultaneously tuneable O vacancy is highly preferred in our design for further charge carrier modulations.

In this work, 2D/2D BiVO<sub>4</sub>/CsPbBr<sub>3</sub> S-scheme heterojunction was successfully fabricated via an in-situ colloidal growth approach. Deep insights into steering charge transfer from the perspectives of interface interaction optimization and IEF modulation towards the as-designed heterojunction were unfolded. By virtue of precisely tuning their contact heterointerface and Fermi level gap, boosted interfacial charge transfer could be realised, contributing to comparably high CO<sub>2</sub>-to-CO conversion with CO yield as high as 103.5 μmol g<sup>-1</sup> with over 97% CO selectivity under visible light irradiation without any co-catalyst or sacrificial agent.

## 2. Experimental section

### 2.1. Reagent and chemicals

Octadecene (ODE, 90%), oleylamine (OM, 70%), oleic acid (OA, 90%), hexane (anhydrous, 95%), bismuth nitrate pentahydrate (Bi(NO<sub>3</sub>)<sub>3</sub>·5H<sub>2</sub>O, 99.99%), ammonium metavanadate (NH<sub>4</sub>VO<sub>3</sub>, 99.9%), lead(II) bromide (PbBr<sub>2</sub>, 99.999% trace metals basis) and caesium

carbonate (Cs<sub>2</sub>CO<sub>3</sub>, 99%) were all purchased from Shanghai Aladdin Bio-Chem Technology Co., Ltd. Dried ODE, OM and OA were obtained by drying corresponding raw materials at 120 °C in a vacuum oven for 1 h.

### 2.2. Sample preparation

#### 2.2.1. Synthesis of BiVO<sub>4</sub> NSs [17]

Approximately 0.242 g of Bi(NO<sub>3</sub>)<sub>3</sub>·5H<sub>2</sub>O was dispersed in a mixture of OA (1 mL), OM (1 mL) and ODE (10 mL) in a three-neck flask. Under the N<sub>2</sub> atmosphere, the flask was heated to 150 °C until a light-yellow transparent solution formed. The temperature was lowered to 100 °C, and 12 mL of 2.4 M HNO<sub>3</sub> aqueous solution containing 0.116 g of NH<sub>4</sub>VO<sub>3</sub> was added dropwise into the above solution, which was maintained for 40 min at 100 °C. Subsequently, the solution was naturally cooled to room temperature, followed by the introduction of a mixture of hexane and ethanol (v/v = 1:1). After stratification, the solution at the upper layer was extracted and centrifuged to remove the residual reactants. The resulting precipitate was washed by a mixture of hexane and ethanol for three times and then dried at 60 °C in an oven for 12 h.

#### 2.2.2. Synthesis of CsPbBr<sub>3</sub> NSs

Firstly, the Cs-OA precursor was prepared. Approximately 0.032 g of Cs<sub>2</sub>CO<sub>3</sub> and 10 mL of dried OA were loaded into a three-neck flask, which was heated to 140 °C under N<sub>2</sub> atmosphere and kept for 30 min. Secondly, 0.026 g of PbBr<sub>2</sub> was loaded to a mixture of dried OA (3 mL), OM (1 mL) and ODE (20 mL). The solution was stirred for 1 h at 120 °C under N<sub>2</sub> atmosphere. The temperature was adjusted to 150 °C, and 2 mL of the above Cs-OA precursor was added dropwise. After finishing the introduction of the Cs-OA precursor, the reaction was maintained for 1 min and then naturally cooled to room temperature. The post-disposal of the resulting products was the same as that of BiVO<sub>4</sub>.

#### 2.2.3. Synthesis of BiVO<sub>4</sub>/CsPbBr<sub>3</sub> NSs

A modified method for the synthesis of CsPbBr<sub>3</sub> NSs with two minor adjustments was used for the synthesis of BiVO<sub>4</sub>/CsPbBr<sub>3</sub> heterojunctions. Firstly, 5 mg of as-obtained BiVO<sub>4</sub> NSs was dispersed in the mixture of dried OA (3 mL), OM (1 mL) and ODE (20 mL) together with 0.026 g of PbBr<sub>2</sub> loading. Secondly, the reaction time was adjusted to 1, 2.5 and 5 min after the introduction of the Cs-OA precursor. BiVO<sub>4</sub>/CsPbBr<sub>3</sub> heterojunctions marked as BC1, BC2 and BC3 were obtained. By annealing as-obtained BiVO<sub>4</sub> NSs at 400 °C under air atmosphere for 1, 2 and 3 h, the BiVO<sub>4</sub> NSs with varying O vacancy concentrations were obtained and named as BiVO<sub>4</sub>-A1, BiVO<sub>4</sub>-A2 and BiVO<sub>4</sub>-A3, respectively. Therefore, similar to the synthetic process of BC2, the BC2-A1, BC2-A2 and BC2-A3 heterojunctions were further obtained.

### 2.3. Characterizations

X-ray diffraction (XRD) pattern was recorded with a Bruker D8 Advance X-ray diffractometer with Cu-Kα radiation at scan range of 5°–80°. Scanning electron microscopy (SEM), transmission electron microscopy (TEM) and atomic force microscopy (AFM) were performed through Gemini SEM 300, Tecnai F20 transmission electron microscope (FEI) and MFP-3D infinity respectively. The UV-vis diffuse reflection spectra (UV-vis DRS) was conducted with assistance of UV-2600 system (Shimadzu). X-ray photoelectron spectroscopy (XPS) and VB-XPS was conducted via Escalab Xi+ (Thermo Scientific). In-situ diffuse reflectance infrared Fourier transform spectroscopy (DRIFTS) was conducted through a Nicolet iS50 FTIR spectrometer (Thermo Fisher, USA). Electron paramagnetic resonance (EPR) spectra were recorded on JEOL JES-FA200 (EPR) at room temperature. The steady-state photoluminescence (PL) and time-resolved transient photoluminescence (TRTPL) emission spectra were tested on FLS-1000 (Edinburgh Instruments). The isotopic experiment was performed on a mass spectrometry (Finnigan MAT 271).

## 2.4. Photocatalytic performance test

An automatic photocatalytic reaction system (Labsolar-6A, Beijing Perfectlight Technology Co., Ltd., China) equipped with gas chromatography (PL9790-II, Zhejiang Fuli Analytical Instruments Co., Ltd., China) was used for photocatalytic reduction of  $\text{CO}_2$  and product analysis. The reactor volume is 350 mL in all, including the custom-made glass vessel sealed with a quartz glass top (250 mL) and the glass piping system (100 mL) of Labsolar-6A. A 300 W Xenon lamp (PLS-SXE300, Perfectlight, China) was used as a light source. Prior to irradiation, the well-dispersed photocatalyst (10 mg) by ultrasonic treatment was uniformly tiled in a Petri dish and then dried in an oven at  $60^\circ\text{C}$ . The dried Petri dish was transferred into a custom-made glass vessel. 500  $\mu\text{L}$  of ultrapure water was injected onto the wall of the glass vessel (not the surface of the photocatalyst), and the vessel sealed with a quartz glass top was evacuated to 1.0 kPa and maintained until the pressure rose to 1.5 kPa. Subsequently,  $\text{CO}_2$  was filled to  $\sim 80$  kPa. The hydrogen and oxygen in the system were determined or qualitatively determined via the gas chromatography (GC-14 C Shimadzu, Japan) with Argon as the carrier gas.

## 2.5. Computational Details

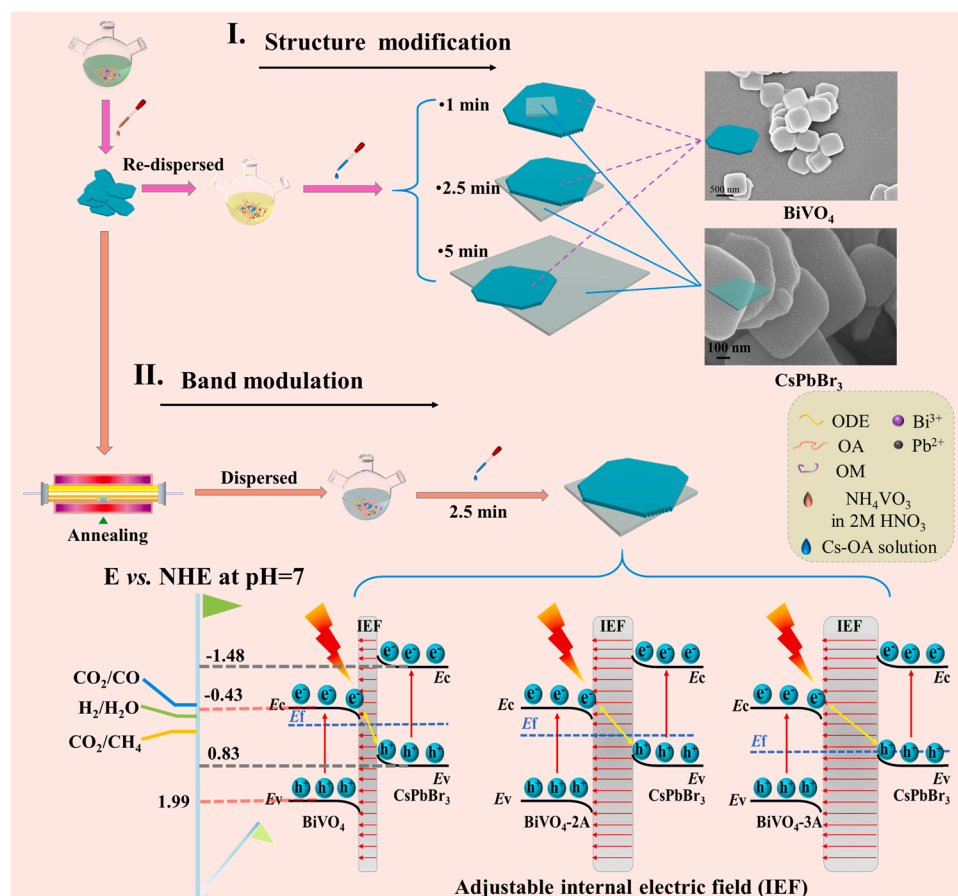
Density functional theory (DFT) calculations were conducted via the Vienna Ab initio Simulation Package (VASP). Generalised gradient approximation in the form of the Perdew–Burke–Erznerhof functional was employed during the calculation process. The  $\text{BiVO}_4$  slab with 25  $\text{BiVO}_4$  formula units (150 atoms in total) was obtained by constructing a  $5 \times 5 \times 1$  supercell after the cleavage of the (020) facet of  $\text{BiVO}_4$  cell. The  $\text{CsPbBr}_3$  slab with 32  $\text{CsPbBr}_3$  formula units (160 atoms in total) was a  $6 \times 6 \times 1$  supercell after the cleavage of the (010) facet of  $\text{CsPbBr}_3$

cell. A  $20 \text{ \AA}$  vacuum layer along the Z direction was created for both  $\text{BiVO}_4$  and  $\text{CsPbBr}_3$  slabs, and the DFT-D3 method was selected to describe the van der Waals interaction. The cut-off energy was set at 400 eV. The energy convergence was set to  $10^{-4}$  eV per atom, and the force convergence was 0.03 eV/ $\text{\AA}$ .

## 3. Results and discussion

### 3.1. Synthesis process and modulation strategies

**Scheme 1** illustrates the synthesis process and modulation operations of the  $\text{BiVO}_4/\text{CsPbBr}_3$  heterojunction. Given the presence of liquid phase in the preparation of  $\text{BiVO}_4$  NSs (details in experimental section) and the instability of  $\text{CsPbBr}_3$  in water, [32,33]  $\text{BiVO}_4$  NSs were synthesized and then used as the substrate for the subsequent growth of  $\text{CsPbBr}_3$ . Two design strategies from the points of structural modification and Fermi level modulation were successively conducted towards the as-synthesized S-scheme  $\text{BiVO}_4/\text{CsPbBr}_3$  heterojunction, both aiming for further steering charge transfer. In Strategy I, by simply altering the growth time, the contact degree of the formed interface was precisely regulated, and three typical types of  $\text{BiVO}_4/\text{CsPbBr}_3$  heterojunctions with different interfacial interaction intensities were obtained. In Strategy II, we tailored the content of intrinsic  $V_{\text{O}}^{\bullet\bullet}$  in  $\text{BiVO}_4$  NSs via the thermal annealing disposal and achieved the gradient Fermi level shift. After reconstruction of  $\text{BiVO}_4/\text{CsPbBr}_3$  heterojunctions, the widened Fermi level gap between  $\text{BiVO}_4$  and  $\text{CsPbBr}_3$  resulted in enhanced IEF at their interface, providing a robust driving force for charge migration.



**Scheme 1.** Schematic illustration of the synthesis, structural modification and band modulation of the  $\text{BiVO}_4/\text{CsPbBr}_3$  heterojunction. 2D  $\text{BiVO}_4$  NSs were synthesised by a colloidal two-phase method with abundant intrinsic  $V_{\text{O}}^{\bullet\bullet}$ . Successive in-situ growth of  $\text{CsPbBr}_3$  NSs could form such three face-to-face heterojunctions by controlling the reaction time while annealing disposal towards  $\text{BiVO}_4$  eliminated  $V_{\text{O}}^{\bullet\bullet}$ , pulling the Fermi level close to the VB position of  $\text{BiVO}_4$ . The depicted Fermi levels are after band alignment.



### 3.2. Verification of the S-scheme charge migration route and their intimate interface

The morphology of as-synthesized  $\text{BiVO}_4/\text{CsPbBr}_3$  heterojunctions was visualised by SEM, TEM and AFM images in Fig. 1 and S1.  $\text{BiVO}_4$  NSs exhibit a 2D quasi-square shape with jagged corners and ‘clean surface’, whilst  $\text{CsPbBr}_3$  NSs exhibit a distinguished perfect 2D square structure with an obvious growth as reference to that of  $\text{BiVO}_4$  NSs (Fig. 1a–d and S2a–S2c; clean surface here means the surface without other small NS fragments attached). Such face-to-face structure is possibly caused by the huge surface energy of  $\text{CsPbBr}_3$  during growth, which drives  $\text{CsPbBr}_3$  attaching onto the  $\text{BiVO}_4$  surface in the solution to maintain the stability of the whole system. [34,35] Pure  $\text{CsPbBr}_3$  NSs possess a quasi-square morphology with random sizes due to the divergent 2D growth orientation (Fig. S2d–S2f). Intriguingly, the presence of the  $\text{BiVO}_4$  substrate could shape the uniformity of  $\text{CsPbBr}_3$  NSs (Fig. 1 and S1). HRTEM shows an obvious interface with two distinguished NSs. The perpendicular lattice fringes with interplanar spacings of 0.26 and 0.25 nm correspond to the (200) and (002) planes of  $\text{BiVO}_4$  NSs, respectively, whereas the lattice fringe of 0.58 nm is for the (001) plane of  $\text{CsPbBr}_3$  (Fig. 1e and S3). Elemental mapping images demonstrate the selective area-concentrated distributions of Bi, V, O, Cs, Pb and Br elements. Coupled with the mixed layer image,  $\text{BiVO}_4$  and  $\text{CsPbBr}_3$  NSs could be further visually distinguished (Fig. 1f). Similarly, AFM exhibits a clear sheet-stacked structure in Fig. 1g and its 3D stereogram in Fig. S4, in which  $\text{BiVO}_4$  and  $\text{CsPbBr}_3$  NSs can be distinguished by their thicknesses from the height cutaway view and the surface potential distribution from the potential cutaway view (inset in Fig. 1g–h). All of these findings collaboratively illustrate the successful construction of a vertical face-to-face  $\text{BiVO}_4/\text{CsPbBr}_3$  structure.

XRD patterns in Fig. 2a demonstrate the pure monoclinic phase of  $\text{BiVO}_4$  NSs (JCPDS:14–0688) [17] and the cubic phase of  $\text{CsPbBr}_3$  NSs (JCPDS:54–0752) [20] highlighted by clubs and diamonds, respectively. Using the DFT calculations, the work functions with a value of 4.78 eV for  $\text{CsPbBr}_3$  NSs and a value of 7.13 eV for  $\text{BiVO}_4$  NSs are determined (Fig. 2b–c; for details, see Fig. S5). Valence band (VB) values are then determined to be 0.83 eV for  $\text{CsPbBr}_3$  and 1.99 eV for  $\text{BiVO}_4$  from VB-XPS analysis (Fig. 2d). [36] After ascertaining their optical band gaps (Eg) from UV-Vis diffuse reflectance spectra, the CB positions of each component are further determined by the transformed Kubelka–Munk function (Fig. 2e). [37–39] The staggered band structure configuration of the  $\text{BiVO}_4/\text{CsPbBr}_3$  heterojunction with obviously distinguished work functions was achieved, meeting the prerequisite for S-scheme heterojunction construction (Fig. 2f). To monitor and verify its charge migration routes, KPFM coupled with an external light source was then adopted to record the potential distribution change of this as-synthesized heterojunction. Without illumination, the potential difference between  $\text{BiVO}_4$  and  $\text{CsPbBr}_3$  NSs is 14.5 mV, which is in good accordance with the value recorded in Figs. 1h and 2g. When irradiated with a 370 nm light source (PEC-10 W) for 10 min, the potential difference at the same selected area gets enlarged to 16.0 mV, illustrating the backward transfer for electrons after light irradiation (Fig. 2i). The detailed charge transfer process is illustrated in Fig. 2h–j. When  $\text{BiVO}_4$  and  $\text{CsPbBr}_3$  NSs came into contact, an IEF directing from  $\text{CsPbBr}_3$  to  $\text{BiVO}_4$  together with band edge bending at the interface was formed during Fermi level alignment due to their different work functions. Upon light irradiation, the photoinduced electrons on the CB of  $\text{BiVO}_4$  and holes on the VB of  $\text{CsPbBr}_3$  recombined with each other under such an IEF, thereby enlarging the potential difference between  $\text{CsPbBr}_3$  and  $\text{BiVO}_4$ . The role changing from electron donor to acceptor for  $\text{CsPbBr}_3$

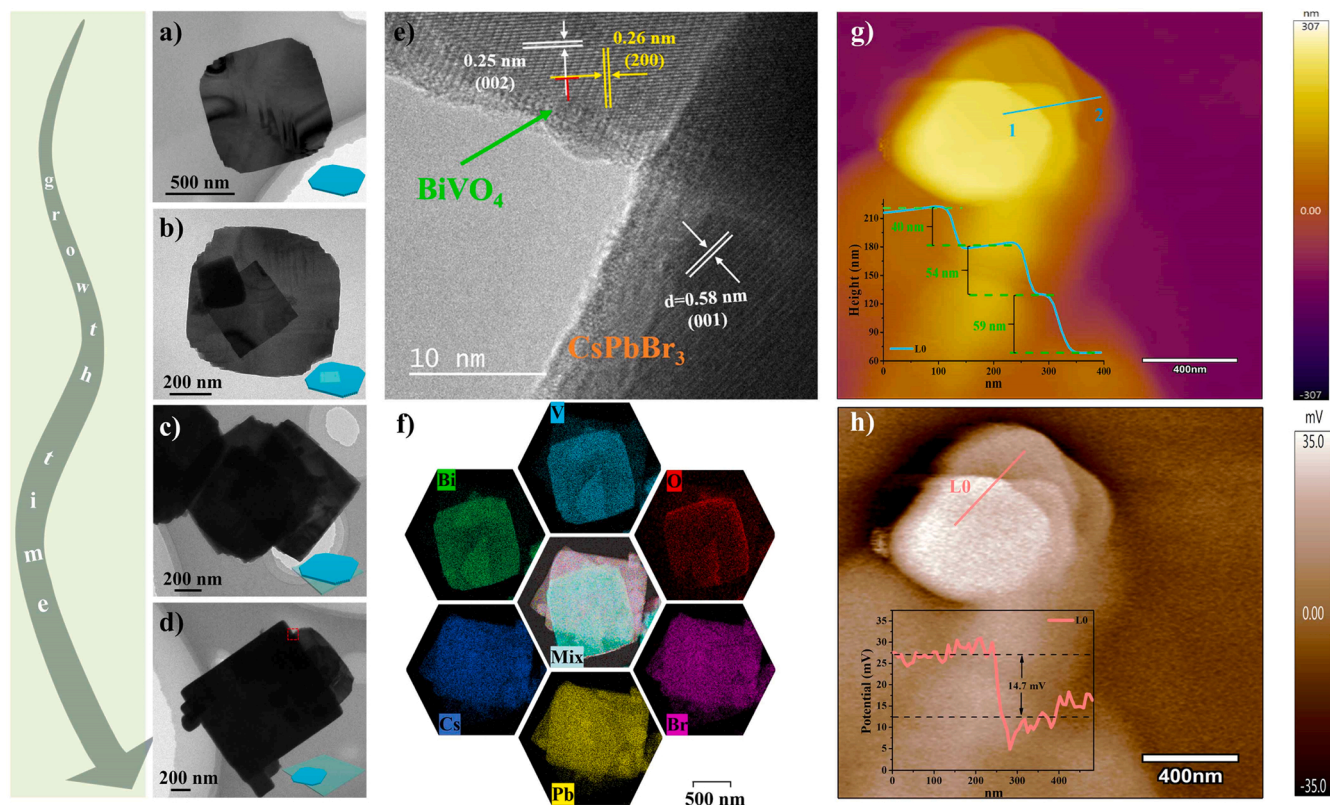


**Fig. 1.** Morphology and AFM characterisations: TEM and HRTEM images of  $\text{BiVO}_4$  (a), BC1(b), BC2 (c) and BC3 (d, e). The corresponding insets illustrate the structural evolution along with the reaction time and HRTEM from the red dotted areas in d; (f) Elemental mapping images for Bi, V, O, Cs, Pb, Br and the Mixed for BC2; (g) AFM of BC2 (Inset in g is the height cutaway view from position 1 to position 2, the thicknesses of these nanosheets are 40, 54 and 59 nm, corresponding to  $\text{CsPbBr}_3$ ,  $\text{BiVO}_4$  and  $\text{BiVO}_4$ , respectively.); (h) Atomic force microscopy images with potential mode (KPFM) for BC2 under dark condition (Inset in h is the potential cutaway view of marked L0, and the potential difference between  $\text{BiVO}_4$  and  $\text{CsPbBr}_3$  NSs is 14.7 mV).



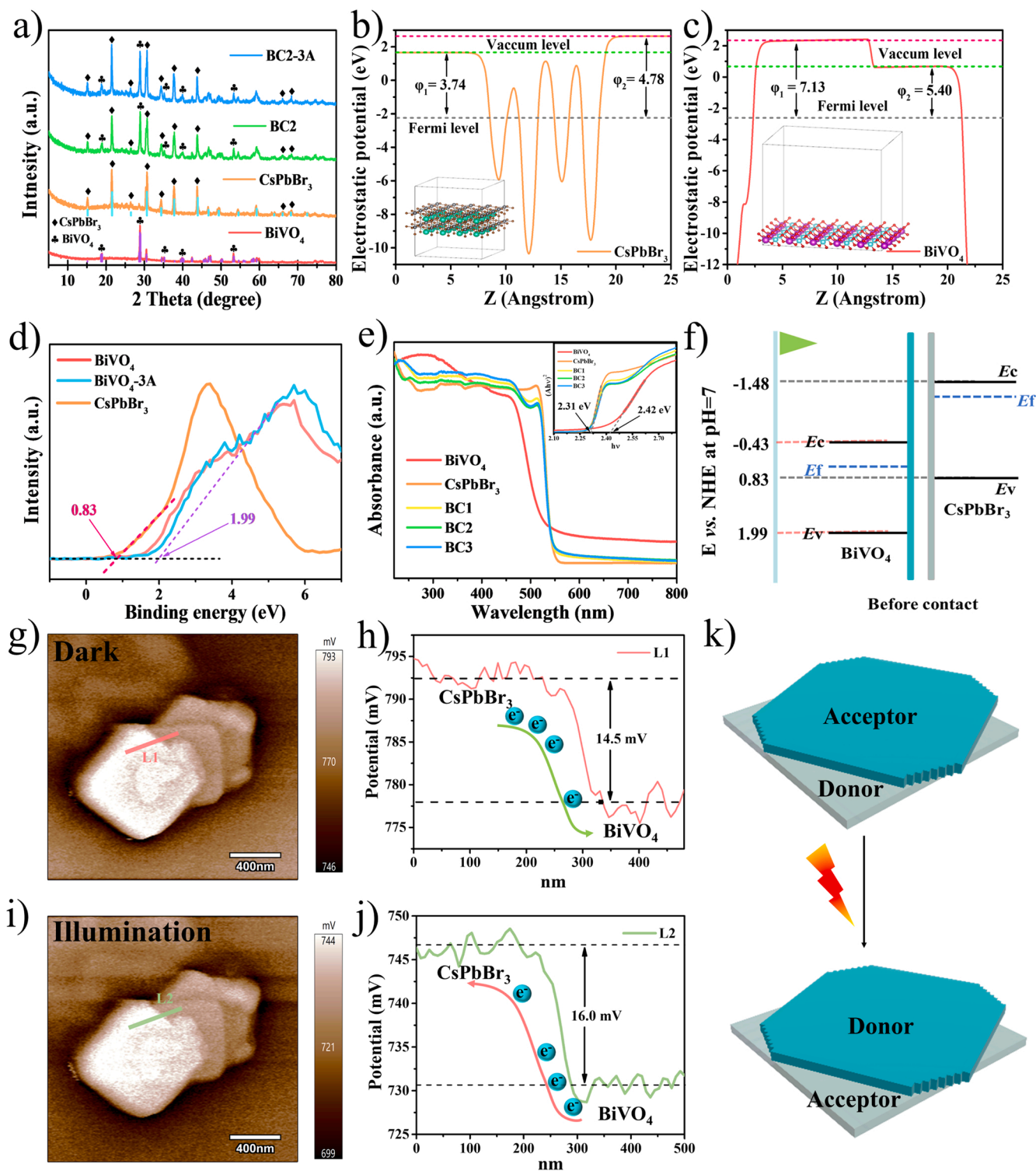


**Fig. 2.** Phase, band structure and electron migration characterisations: (a) XRD patterns of as-prepared samples; (b and c) Electrostatic potentials of the CsPbBr<sub>3</sub> (010) surface and BiVO<sub>4</sub> (020) surface along the Z-axis direction. The insets in (b) and (c) are the optimised slab structures of CsPbBr<sub>3</sub> and BiVO<sub>4</sub> NSs, respectively. (d) Valence-band XPS of BiVO<sub>4</sub>, BiVO<sub>4</sub>-3A and CsPbBr<sub>3</sub>; (e) UV-Vis diffuse reflectance spectra of as-synthesised samples. The inset in (e) displays the band gap values estimated from the plotted curves of  $(\alpha h\nu)^2$  vs  $h\nu$ ; (f) Illustration of band structures of BiVO<sub>4</sub> and CsPbBr<sub>3</sub> before contact; KPFM for BC2 under (g) dark condition and (i) 370 nm light irradiation for 10 min; (h) and (j) are the potential cutaway views of marked L1 and L2 in (g) and (i), respectively; (k) Change illustration from donor to acceptor for CsPbBr<sub>3</sub> after light irradiation: The intimate contact of BiVO<sub>4</sub> and CsPbBr<sub>3</sub> induced Fermi level alignment with CsPbBr<sub>3</sub> as electron donor, forming an IEF at the interface, which pulled the excited electrons on the CB of BiVO<sub>4</sub> to recombine with the holes on the VB of CsPbBr<sub>3</sub> as acceptor upon light irradiation.

before and after light irradiation occurred during the above processes (Fig. 2k). Coupled with photo-irradiated KPFM characterisation, the 2D/2D BiVO<sub>4</sub>/CsPbBr<sub>3</sub> heterojunction with an S-scheme charge migration route is confirmed.

In XPS analysis (Fig. 3, S5 and S6), Fig. 3a shows the Bi 4f high-resolution spectra of BiVO<sub>4</sub> and BiVO<sub>4</sub>/CsPbBr<sub>3</sub> heterojunction. Two typical spin-orbit splitting peaks centred at 159.1 and 164.4 eV with a standard 5.3 eV splitting energy ( $\Delta$ ) correspond to trivalent bismuth, both of which exhibit a 0.6 eV shift to low binding energy after heterojunction construction. Fig. 3b exhibits a 0.3 eV shift to high binding energy for V 2p with a characteristic 7.6 eV  $\Delta$  and a 0.3 eV shift to low binding energy for O 2p, suggesting the charge redistribution of BiVO<sub>4</sub> originated from the firm interface between BiVO<sub>4</sub> and CsPbBr<sub>3</sub> NSs. Similarly, a 0.3 eV shift to high binding energy for Cs 3d and intensified spin-orbit splitting function of Br 3d with the increased  $\Delta$  value from 1.03 eV to 1.08 eV can be clearly observed in Fig. 3c-d. This phenomenon indicates the electron consumption on Cs and relative accumulation on Br, which is conducive to the chemisorption of CO<sub>2</sub>. For example, C bonded with Br, O bonded with Cs chemisorption model or two O atoms of a CO<sub>2</sub> molecular bonded with the Cs model. [40] The strong electron transfer behaviour between BiVO<sub>4</sub> and CsPbBr<sub>3</sub> NSs illustrates the formation of an intimate interface with intensive interfacial interaction.

### 3.3. Further steering charge transfer from the regulation on interfacial interaction: Revelation of structure-activity characteristics

The regulated interface interaction intensity abided by their different structures (namely BC1, BC2 and BC3) was accurately evaluated by the effective contact ratio ( $R_{eff}$ ) calculated via the following Eq. (1):

$$R_{eff} = \frac{A_{con}/A_1 + A_{con}/A_2}{2} \times 100\% \quad (1)$$

$A_1$  and  $A_2$  are areas of contact planes of BiVO<sub>4</sub> and CsPbBr<sub>3</sub>, respectively, and  $A_{con}$  is area of the interface. The denominator '2' represents the equivalent role for BiVO<sub>4</sub> and CsPbBr<sub>3</sub> in the

heterojunction. To obtain rational  $R_{eff}$ , we chose at least three morphological images for each type structure (Fig. 4a and Fig. S7), and corresponding located  $R_{eff}$  ranges are depicted in Fig. 4b. Obviously, BC2 possesses the highest  $R_{eff}$  ranging from 58.6% to 87.0%, indicating the strongest interaction at the interface. Such an intensive interaction largely improves the charge diffusion and transfer capability, which is further verified from time-resolved photoluminescence (TRPL) spectroscopy. [41,42] As shown in Fig. 4c and Table 1, the estimated average decay lifetime ( $\tau_{ave}$ ) of pure CsPbBr<sub>3</sub> is determined to 3.65 ns, comparable with their nanocubes (average lifetime of 1–22 ns) and thin films (average lifetime of ~3.9 ns). [43] The obviously shortened  $\tau_{ave}$  values (1.20, 1.53 and 1.73 ns for BC1, BC2 and BC3, respectively) indicate the emergence of the non-radiative pathway for excited electrons, which are beneficial for efficient charge separation. [20,44] The anomalous value for BC1 may be ascribed to the quantum size effect by some CsPbBr<sub>3</sub> NSs with tiny size.

Photocatalytic CO<sub>2</sub> reduction was conducted as a probe reaction to check the validity of accelerated dynamic carrier mobility under visible light irradiation without introducing any sacrificial agent or cocatalyst. Control experiments without the use of catalysts (BC2) or light or CO<sub>2</sub> source were firstly performed and no related products were detected, indicating their indispensable necessity for achieving CO<sub>2</sub> reduction (Fig. S8). As shown in Fig. S9a, benefiting from the construction of S-scheme heterojunction, all the heterojunctions show an obvious improvement in the recorded CO yields (CO is the main product). Moreover, a continuous increase without obvious decay within 4 h for all the as-design heterojunctions can be observed, indicating their much more robust photocatalytic activity than those of pure CsPbBr<sub>3</sub> and BiVO<sub>4</sub> with a slowed up-climbing trend after the third hour. Amongst these heterojunctions, BC2 presents the highest activity with nearly 68  $\mu\text{mol g}^{-1}$  CO yield in 4 hrs, with 20.3% and 24.7% increases compared with those of BC1 and BC3, which is in good consistent with the results from the structure regulation design. Notably, BC2 shows ~61.5% and 201.7% increase when compared with pure CsPbBr<sub>3</sub> NSs (41.90  $\mu\text{mol g}^{-1}$ ) and BiVO<sub>4</sub> NSs (22.42  $\mu\text{mol g}^{-1}$ ), respectively (Fig. S9b). Besides, a same trend to CO yield can be also observed in selectivity for these as-

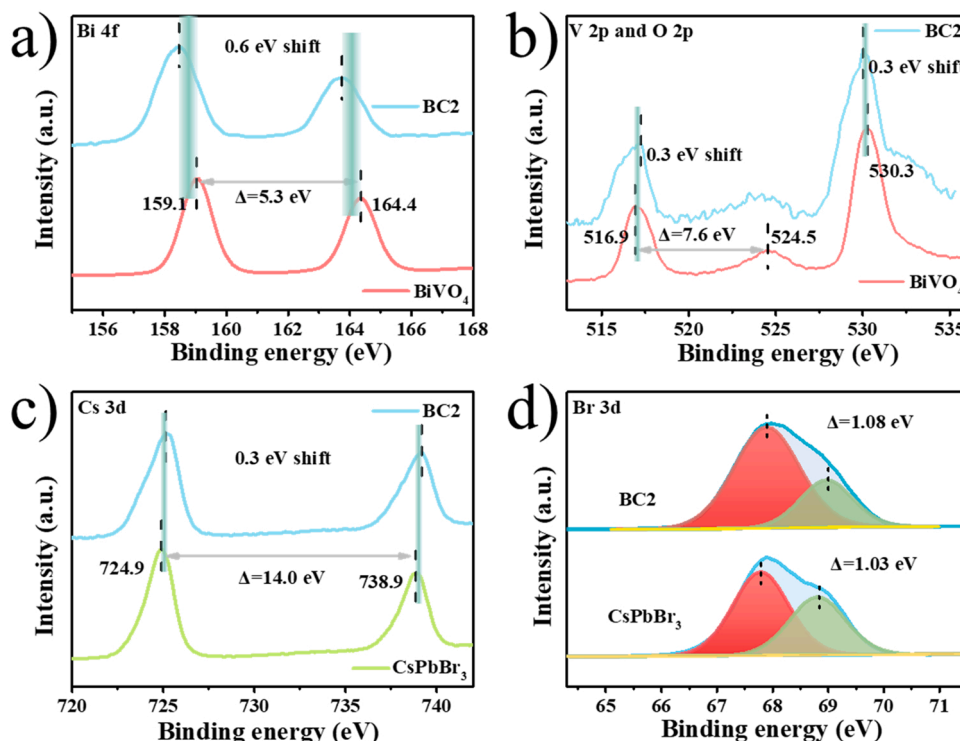
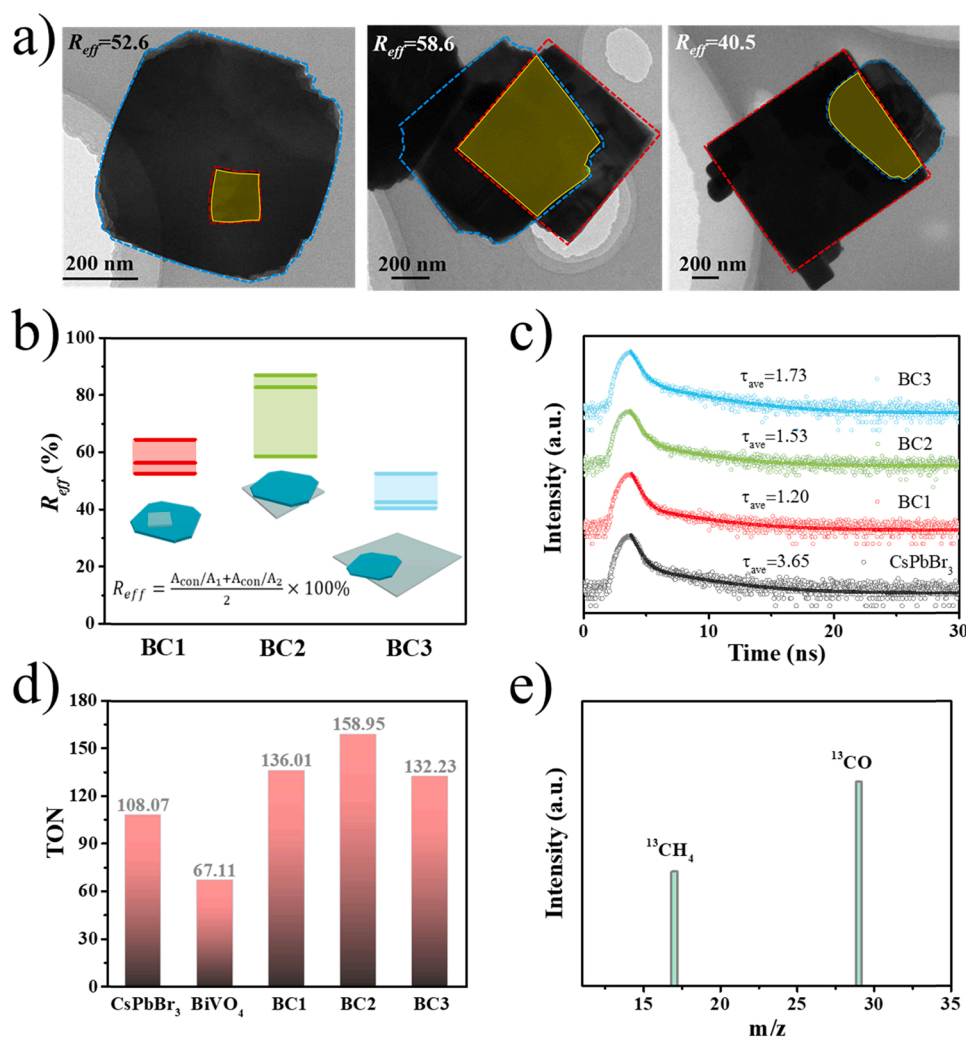


Fig. 3. XPS characterisations: high-resolution XPS spectra of (a) Bi 4f, (b) V and O 2p, (c) Cs 3d and (d) Br 3d for BiVO<sub>4</sub>, CsPbBr<sub>3</sub> and BC2.



**Fig. 4. Comparable photocatalytic CO<sub>2</sub> reduction performance of as-synthesised photocatalysts: (a)** Three different structures with corresponding  $R_{eff}$  values and **(b)** Statistical  $R_{eff}$  distributions for BiVO<sub>4</sub>/CsPbBr<sub>3</sub> heterojunctions; **(c)** Time-resolved transient PL spectra of the light emission at 532 nm from CsPbBr<sub>3</sub>, BC1, BC2 and BC3, excitation wavelength: 450 nm; **(d)** TONs of as-synthesised photocatalysts; **(e)** The mass spectra of <sup>13</sup>CO and <sup>13</sup>CH<sub>4</sub> generated in the photocatalytic reduction of <sup>13</sup>CO<sub>2</sub>.

**Table 1**

Tri-exponential decay time constants of time-resolved transient PL acquired from as-synthesized photocatalysts.

Sample	$\tau_1$ /ns (A1)	$\tau_2$ /ns (A2)	$\tau_3$ /ns (A3)	$\tau_{ave}$ /ns	R <sup>2</sup>
CsPbBr <sub>3</sub>	32.29 (2.69)	2.42 (91.62)	0.29 (2304.32)	3.65	0.9997
BC1	0.42 (383.03)	0.42 (538.21)	2.69 (75.34)	1.20	0.9998
BC2	0.46 (451.47)	0.46 (437.63)	2.95 (104.45)	1.53	0.9998
BC3	0.48 (435.41)	0.48 (390.07)	3.27 (97.21)	1.73	0.9997
BC2-3A	0.44 (506.70)	2.84 (85.85)	0.44 (401.05)	1.35	0.9994

$\tau_{ave}$  is calculated via the following equation:

$$\tau_{ave} = \frac{A_1 \tau_1^2 + A_2 \tau_2^2 + A_3 \tau_3^2}{A_1 \tau_1 + A_2 \tau_2 + A_3 \tau_3} \quad (2)$$

designed samples. An over 95% CO selectivity with the highest TON value of nearly 159 can be achieved by BC2 (Fig. S9c and Fig. 4d). Subsequent recycling tests demonstrate that BC2 possesses high stability in first two cycles (Fig. S10). The activity at the second cycle even has a little increase. After that, it comes to decrease. It is worth noting that the CO yield after the fourth cycle is still higher than those of pure BiVO<sub>4</sub> and CsPbBr<sub>3</sub>. The continuous decrease for the third and fourth cycles may be ascribed to the decomposition process of CsPbBr<sub>3</sub> under the H<sub>2</sub>O (g) atmosphere. To clearly illustrate this speculation, the morphology of BC2 photocatalyst after four recycling tests was further characterized by

TEM. As shown in Fig. S11, the 2D/2D face-to-face heterostructure could be still clearly observed. However, it can be also observed that the corner of CsPbBr<sub>3</sub> NSs is not as sharp as its initial stage, which is ascribed to the influence of the H<sub>2</sub>O(g) atmosphere during the recycling tests. Such TEM result is in good accordance with our speculation. To confirm the carbon source in reductive products, the isotopic experiment with the isotopic <sup>13</sup>CO<sub>2</sub> as the reactant was performed in the photocatalytic reaction. As shown in Fig. 4e, both the converted <sup>13</sup>CO ( $m/z = 29$ ) and <sup>13</sup>CH<sub>4</sub> ( $m/z = 17$ ) can be clearly detected, verifying that these reductive products are originated from the photocatalytic CO<sub>2</sub> conversion process. To further reflect the superiority of the as-designed 2D/2D BiVO<sub>4</sub>/CsPbBr<sub>3</sub>, 2D/0D BiVO<sub>4</sub>/CsPbBr<sub>3</sub> was synthesized for comparison. As shown in Fig. S12b-c, the 0D CsPbBr<sub>3</sub> nanoparticles are successfully synthesized with a mean diameter of 40.2 nm. And as the same feed amounts as BC2, the 0D CsPbBr<sub>3</sub> nanoparticles are in-situ grown onto BiVO<sub>4</sub> NSs, forming the 2D/0D BiVO<sub>4</sub>/CsPbBr<sub>3</sub> heterojunction (Fig. S12d-e). Photocatalytic CO<sub>2</sub> reduction experiments show that the average yield rate of the main product (CO) could only reach 10.77  $\mu\text{mol g}^{-1} \text{h}^{-1}$ , which is less than that of BC2 (16.91  $\mu\text{mol g}^{-1} \text{h}^{-1}$ ) (Fig. S12f). Furthermore, from the result of the comparable CH<sub>4</sub>, the CO selectivity of BC2 also outperforms that of 2D/0D BiVO<sub>4</sub>/CsPbBr<sub>3</sub>. Based on these above results, boosted charge migration can be realized for effective photocatalytic CO<sub>2</sub> conversion by structural regulation towards as-designed S-scheme heterojunctions.



### 3.4. Further steering charge transfer from enhancing IEF by Fermi level modulation

The above design aimed to alter the interfacial interaction of BiVO<sub>4</sub>/CsPbBr<sub>3</sub> heterojunctions to achieve an intimate interface for more effective charge migration. By contrast, this section aimed at modulating the essential IEF intensity at the intimate interface to further steer charge transfer. Such modulation can be achieved by enlarging the Fermi level gap of BiVO<sub>4</sub> and CsPbBr<sub>3</sub> via regulating the intrinsic  $V_O^{\bullet\bullet}$  of as-obtained BiVO<sub>4</sub> NSs. EPR characterisation (Fig. 5a) shows gradually decreased signal intensity located at  $g = 2.003^{17}$ , suggesting the gradual removal of  $V_O^{\bullet\bullet}$  by the annealing disposal (BiVO<sub>4</sub>-2A was annealed for 2 h, and BiVO<sub>4</sub>-3A for 3 h). It is known that the flat band potential of the n-type semiconductor is equal to its Fermi level, [45,46] therefore Mott–Schottky test was performed for accurately determining the Fermi levels of the as-synthesized raw and annealed BiVO<sub>4</sub> NSs. The flat potentials in Fig. 5b are calculated to be  $-0.57$ ,  $-0.47$  and  $-0.37$  eV versus the Ag/AgCl electrode for BiVO<sub>4</sub>, BiVO<sub>4</sub>-2A and BiVO<sub>4</sub>-3A, respectively. The positive shift of the flat potential indicates the downshift of Fermi level, thus enlarging their Fermi level gap between BiVO<sub>4</sub> and CsPbBr<sub>3</sub> (Fig. 5c and d). Notably, the intact 2D structure of BiVO<sub>4</sub> can be still reserved after annealing from its TEM images (insets in Fig. 5c and S13). The reconstructed heterojunctions (BC2-A2 and BC2-A3) show an obvious gradient increase on photocatalytic CO<sub>2</sub> reduction under the same testing condition, except for a slight weak

attenuation for BC2-A1 compared with BC2, which may be attributed to the removal of the organic species attached on the surface, not  $V_O^{\bullet\bullet}$  due to short annealing time (Fig. 5e). Specifically, the CO yield of BC2-A3 reaches  $103.5 \mu\text{mol g}^{-1}$ , with further increases of  $\sim 53\%$ ,  $147\%$  and  $362\%$  compared with those of BC2, CsPbBr<sub>3</sub> and BiVO<sub>4</sub>, respectively. Such outstanding enhancement based on the optimal heterojunction structure demonstrates the validity of  $V_O^{\bullet\bullet}$  removal as assumed. The activity for the annealed BiVO<sub>4</sub> shows a decrease in the yields of both CO and CH<sub>4</sub> products, which further illustrates the superiority of Fermi level modulation in such S-scheme heterojunction (for details, see Fig. S14). Besides, we encouragingly found a gradual decrease in the CH<sub>4</sub> yield rate along with the prolongation of annealing pre-treatment towards BiVO<sub>4</sub> NSs, thereby increasing CO selectivity of as-obtained BC2, BC2-A1, BC2-A2 and BC2-A3 with values of 95.8%, 95.8%, 96.5% and 97.4%, respectively (Fig. 5e and S15). Such phenomenon is ascribed to the presence of  $V_O^{\bullet\bullet}$ , which is thermodynamically favourable for the hydrogenation process of  $^*\text{CHO}$  to CH<sub>4</sub> (“\*” represents adsorption sites). [41] Besides the high CO selectivity of over 97%, BC2-A3 possesses the highest TON value of 229.35, indicating its superior photocatalytic activity towards CO<sub>2</sub> reduction (Fig. S15). The intensified IEF at the interface would drive the recombination of the useless carriers in an accelerated way, resulting in much higher charge separation efficiency, which is verified by the shortened average decay lifetime (1.35 ns) than that of BC2 (1.53 ns; Fig. 5f). This intensified IEF will also endow the intimate interface with much stronger interfacial interaction between

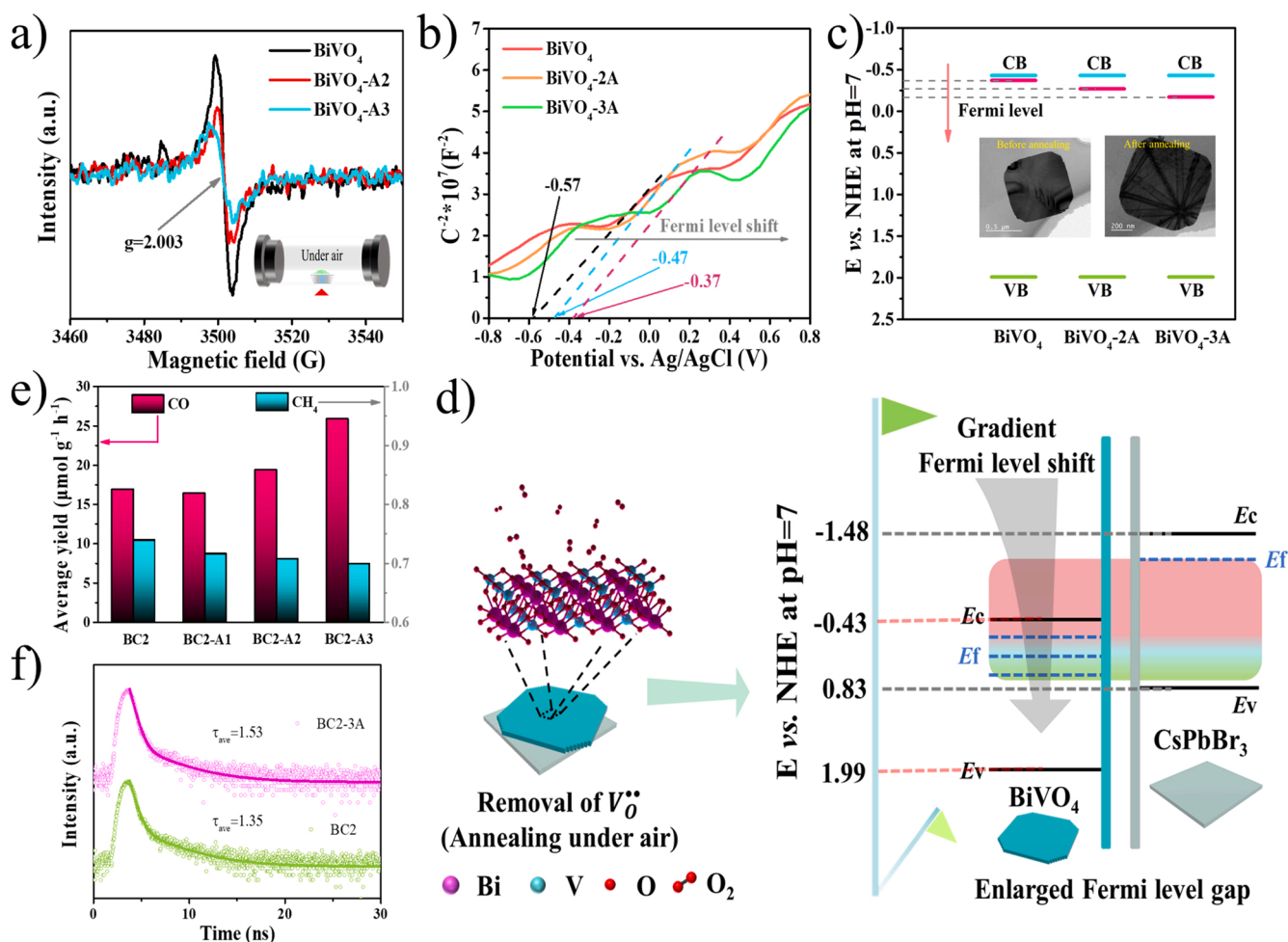


**Fig. 5. Performance test and certification of Fermi level shift:** (a) EPR spectra of BiVO<sub>4</sub>, BiVO<sub>4</sub>-A2 and BiVO<sub>4</sub>-A3; (b) Mott–Schottky plots of BiVO<sub>4</sub>, BiVO<sub>4</sub>-2A and BiVO<sub>4</sub>-3A versus the Ag/AgCl electrode in 0.1 M Na<sub>2</sub>SO<sub>4</sub>; (c) Fermi level shift versus NHE at pH= 7; (d) Illustration of the enlarged Fermi level gap between BiVO<sub>4</sub> and CsPbBr<sub>3</sub> from  $V_O^{\bullet\bullet}$  regulation towards BiVO<sub>4</sub> NSs; (e) CO yield versus time over different photocatalysts; (f) Time-resolved transient PL spectra of the light emission at 532 nm from BC2–3A (excitation wavelength: 450 nm).

$\text{BiVO}_4\text{-A3}$  and  $\text{CsPbBr}_3$ , which was verified from XPS measurements (for details, Fig. S16). Such results further proved the rationality of the design strategy on interfacial interaction regulation.

### 3.5. Evolution of surface intermediates and photocatalytic mechanism

In-situ diffuse reflectance infrared Fourier transform spectroscopy (DRIFTS) measurements under dark (0–20 min) and light irradiation (0–20 min, 365 nm Xenon lamp) environments were performed to track and record the complicated adsorbed species and intermediates in the processes of adsorption, activation and conversion of  $\text{CO}_2$ . Under dark environment within 20 min, the adsorbed species and/or intermediates such as  $\text{CO}_2$ ,  $\text{CO}_3^{2-}$  and  $\text{HCO}_3^-$  could still be tracked despite weak signal change (Fig. S16). When exposed under light irradiation, the dynamic floating of the curves became more active, indicating the quick photo-conversion process of these adsorbed species and intermediates over the

photocatalysts. Specifically, as shown in Fig. 6a and c, monodentate carbonate ( $\text{m-CO}_3^{2-}$ ,  $\nu_s(\text{CO}_3)$ : 1380 and 1476  $\text{cm}^{-1}$ ), bidentate carbonate species ( $\text{b-CO}_3^{2-}$ ,  $\nu_s(\text{CO}_3)$ : 1347  $\text{cm}^{-1}$ ,  $\nu_{as}(\text{CO}_3)$ : the range of 1560–1599  $\text{cm}^{-1}$ ) and chelating-bridged carbonate ( $\text{c-CO}_3^{2-}$ ,  $\nu(\text{C-O})$ : 1733  $\text{cm}^{-1}$ ) can be clearly detected for both BC2 and BC2-3A. [40,47] From their high-resolution spectra (Fig. 6c and d), most of the carbonate species of BC2 display a gradual enhanced signal response in 20 min, whereas the signal response for those of BC2-3A is enhanced first and then decreased in 20 min, corresponding to successive adsorption, activation and conversion. Besides, the signals of  $\text{m-CO}_3^{2-}$  and  $\text{c-CO}_3^{2-}$  for BC2 are stronger and much more visually obvious than that of BC2-3A, it may be ascribed to the presence of much more  $\text{V}_O^{\bullet}$  of BC2, which could act as a catalytic site for absorbing  $\text{CO}_2$  in a monodentate or chelating-bridge manner. [40,48] However, such absorbed  $\text{CO}_2$  needs to consume much more time and energy to accomplish absolute protonation due to weak single-site bonding, which impedes the activation and

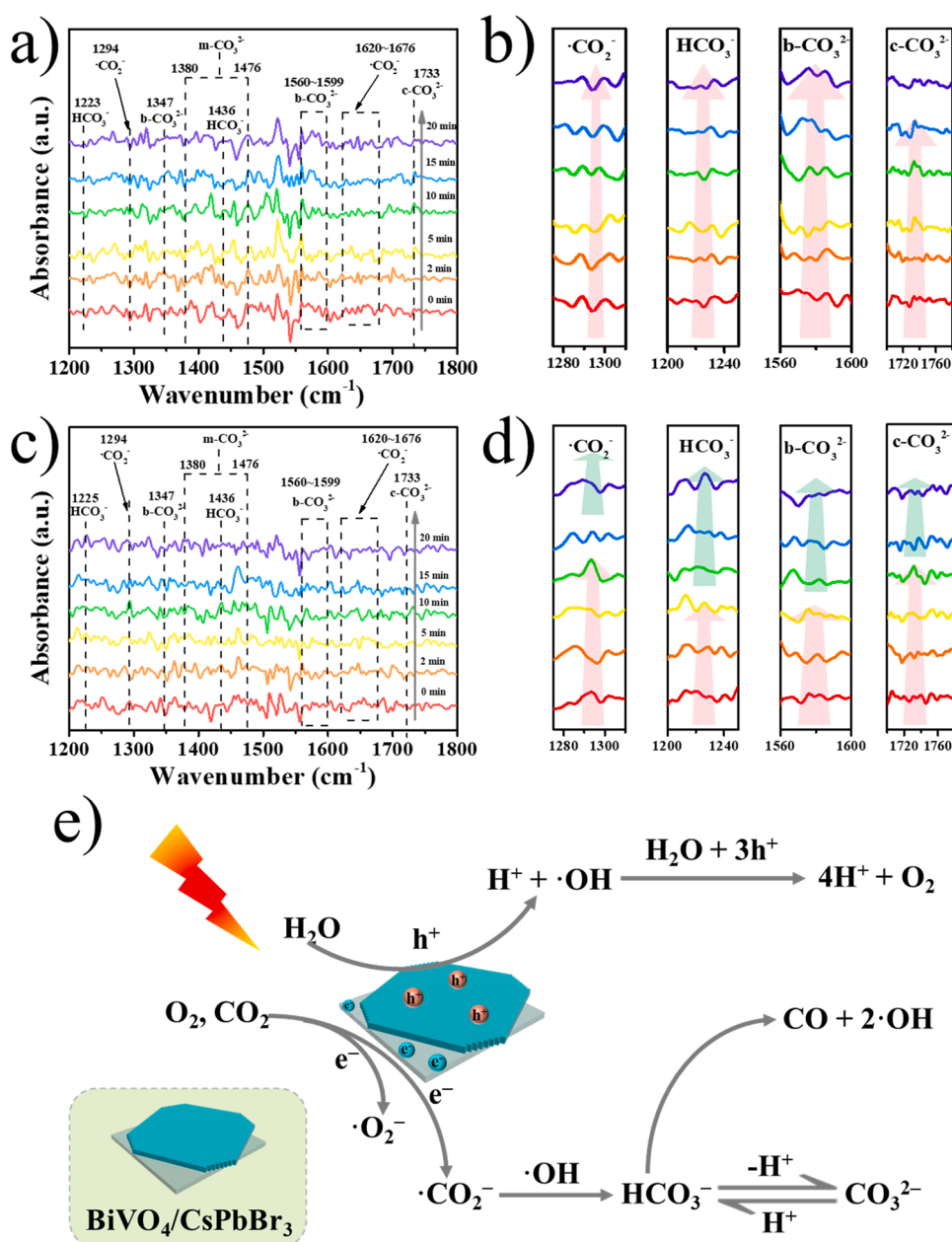


**Fig. 6.** In-situ DRIFTS measurements for  $\text{CO}_2$  and  $\text{H}_2\text{O}$  interaction with (a) BC2 and (c) BC2-3A under 365 nm light irradiation for 20 min; (b, d) Corresponding high-resolution spectra of several typical intermediates; (e) Proposed mechanism of  $\text{CO}_2$  photocatalysis under visible-light irradiation over the  $\text{BiVO}_4/\text{CsPbBr}_3$  heterojunction.

hydrogenation efficiencies during photocatalytic CO<sub>2</sub> reduction. Another important kind of intermediate is the bicarbonate species. The peaks at 1222 and 1436 cm<sup>-1</sup> are assigned to  $\delta_{\text{OH}}$  and  $\nu_{\text{as}}(\text{CO}_3)$  modes originating from the bicarbonates. [49] Similar evolution phenomenon can be also observed for bicarbonate species (for details, please refer to Fig. S17). All of these results indicate that BC2-3A exhibits a more effective catalytic process than BC2, which is in good consistent with the above experimental results and design operations. Furthermore, to reveal the mechanism of CO<sub>2</sub> photoreduction over as-designed photocatalysts, the detection of H<sub>2</sub> for all the samples and the qualitative evaluation on O<sub>2</sub> for the optimal BC2-A3 were carried out. No detectable H<sub>2</sub> could be observed for all the as-designed samples, indicating its negligible competitiveness at the reduction half-reaction during CO<sub>2</sub> photoreduction process. While for the detection of O<sub>2</sub>, it is found that the O<sub>2</sub> yield decreased first and then increased (Fig. S18). The initial O<sub>2</sub> is originated from the input high-purity CO<sub>2</sub>. At the initial stage (the beginning 2 h), the reaction ( $\text{O}_2 + \text{e}^- \rightarrow \cdot\text{O}_2^-$ ) could act as a competitive reaction to CO<sub>2</sub> photoreduction, during which the consumption rate of O<sub>2</sub> is over its production rate, thus the decrease appears. After that, corresponding production rate exceeds the consumption rate, thereby an obvious increased O<sub>2</sub> signal appears. Based on the above results and analysis, the mechanism of CO<sub>2</sub> photoreduction over the BiVO<sub>4</sub>/CsPbBr<sub>3</sub> photocatalyst is depicted in Fig. 6e.

#### 4. Conclusion

In conclusion, a 2D/2D BiVO<sub>4</sub>/CsPbBr<sub>3</sub> vertical heterojunction was precisely fabricated with designed S-scheme charge transfer mechanism ascribed to the distinguished work functions and staggered band structures, confirmed by DFT calculations, TRPL spectroscopy, XPS and photo-irradiated Kelvin probe measurements. In-depth modulations on further steering dynamic charge transfer towards the as-designed photocatalyst were successfully operated from perspectives of intensifying interfacial interaction and enhancing the IEF at the interface. Different interfacial interaction intensities endowed by the heterojunction structures are accurately evaluated by establishing the parameter  $R_{\text{eff}}$ . Profiting from the intensified interfacial interaction, BC2 with the highest  $R_{\text{eff}}$  demonstrates superior photocatalytic activity among three researched types of BiVO<sub>4</sub>/CsPbBr<sub>3</sub> heterojunctions. IEF modulation are based on the optimal heterojunction structure by enlarging their Fermi level gap via regulation on the intrinsic  $V_{\text{O}}^{\bullet\bullet}$  of as-obtained BiVO<sub>4</sub> NSs. Hence, boosted charge transfer migration for photocatalytic CO<sub>2</sub> reduction can be realised. The CO yield of BC2-3A reaches as high as 103.5  $\mu\text{mol g}^{-1}$  with over 97% CO selectivity under visible light irradiation without any co-catalyst or sacrificial agent. This work paves an avenue for the rational design of 2D/2D S-scheme heterojunctions and more in-depth design on carrier transfer modulation towards high-efficiency photocatalysts.

#### CRedit authorship contribution statement

**Xiaoyang Yue:** Methodology, Visualization, Writing – original draft, Investigation. **Lei Cheng:** Writing – review & editing, Data curation. **Jiajie Fan:** Data curation, Conceptualization. **Quanjun Xiang:** Supervision, Writing – review & editing, Funding acquisition.

#### Declaration of Competing Interest

The authors declare that they have no known competing financial interests or personal relationships that could have appeared to influence the work reported in this paper.

#### Acknowledgements

This work was partially supported by the National Natural Science Foundation of China under Grant No. 51672099 and 52073263, Sichuan

Science and Technology Program under No. 2021JDTD0026, Fundamental Research Funds for the Central Universities under No. 2017-QR-25.

#### Appendix A. Supporting information

Supplementary data associated with this article can be found in the online version at doi:10.1016/j.apcatb.2021.120979.

#### References

- [1] X. Li, J. Yu, M. Jaroniec, X. Chen, Cocatalysts for selective photoreduction of CO<sub>2</sub> into solar fuels, *Chem. Rev.* 119 (2019) 3962–4179.
- [2] Y. Li, B. Li, D. Zhang, L. Cheng, Q. Xiang, Crystalline carbon nitride supported copper single atoms for photocatalytic CO<sub>2</sub> reduction with nearly 100% CO selectivity, *ACS Nano* 14 (2020) 10552–10561.
- [3] X.J. Wu, J. Chen, C. Tan, Y. Zhu, Y. Han, H. Zhang, Controlled growth of high-density CdS and CdSe nanorod arrays on selective facets of two-dimensional semiconductor nanoplates, *Nat. Chem.* 8 (2016) 470–475.
- [4] F. Chen, H. Huang, L. Ye, T. Zhang, X. Han, T. Ma, Thickness-dependent facet junction control of layered BiOI/O<sub>3</sub> single crystals for highly efficient CO<sub>2</sub> photoreduction, *Adv. Funct. Mater.* 28 (2018), 1804284.
- [5] Y. Xiao, C. Feng, J. Fu, F. Wang, C. Li, V. Kunzelmann, C. Jiang, M. Nakabayashi, N. Shibata, I. Sharp, K. Domen, Y. Li, Band structure engineering and defect control of Ta<sub>3</sub>N<sub>5</sub> for efficient photoelectrochemical water oxidation, *Nat. Catal.* 3 (2020) 932–940.
- [6] S. Bai, N. Zhang, C. Gao, Y. Xiong, Defect engineering in photocatalytic materials, *Nano Energy* 53 (2018) 296–336.
- [7] R. Ye, J. Zhao, B.B. Wickemeyer, F.D. Toste, G.A. Somorjai, Foundations and strategies of the construction of hybrid catalysts for optimized performances, *Nat. Catal.* 1 (2018) 318–325.
- [8] M. Zhu, Z. Sun, M. Fujitsuka, T. Majima, Z-Scheme photocatalytic water splitting on a 2D heterostructure of black phosphorus/bismuth vanadate using visible light, *Angew. Chem. Int. Ed.* 57 (2018) 2160–2164.
- [9] L. Cheng, Q. Xiang, Y. Liao, H. Zhang, CdS-Based photocatalysts, *Energy Environ. Sci.* 11 (2018) 1362–1391.
- [10] X. Xia, J. Pan, L. Hu, J. Yao, Y. Ding, D. Wang, J. Ye, S. Dai, Photochemical conversion and storage of solar energy, *ACS Energy Lett.* 4 (2019) 405–410.
- [11] Q. Xu, L. Zhang, B. Cheng, J. Fan, J. Yu, S-scheme heterojunction photocatalyst, *Chem* 6 (2020) 1543–1559.
- [12] C. Cheng, B. He, J. Fan, B. Cheng, S. Cao, J. Yu, An inorganic/organic S-scheme heterojunction H<sub>2</sub>-production photocatalyst and its charge transfer mechanism, *Adv. Mater.* 33 (2021), 2100317.
- [13] P. Xia, S. Cao, B. Zhu, M. Liu, M. Shi, J. Yu, Y. Zhang, Designing a 0D/2D S-scheme heterojunction over polymeric carbon nitride for visible-light photocatalytic inactivation of bacteria, *Angew. Chem. Int. Ed.* 59 (2020) 5218–5225.
- [14] X. Tao, Y. Gao, S. Wang, X. Wang, Y. Liu, Y. Zhao, F. Fan, M. Dupuis, R. Li, C. Li, Interfacial charge modulation: An efficient strategy for boosting spatial charge separation on semiconductor photocatalysts, *Adv. Energy Mater.* 9 (2018), 1803951.
- [15] C. Li, S. Yi, Y. Liu, Z. Niu, X. Yue, Z. Liu, In-situ constructing S-scheme/Schottky junction and oxygen vacancy on SrTiO<sub>3</sub> to steer charge transfer for boosted photocatalytic H<sub>2</sub> evolution, *Chem. Eng. J.* 417 (2021), 129231.
- [16] R. Li, H. Han, F. Zhang, D. Wang, C. Li, Highly efficient photocatalysts constructed by rational assembly of dual-cocatalysts separately on different facets of BiVO<sub>4</sub>, *Energy Environ. Sci.* 7 (2014) 1369–1376.
- [17] C. Dong, S. Lu, S. Yao, R. Ge, Z. Wang, Z. Wang, P. An, Y. Liu, B. Yang, H. Zhang, Colloidal synthesis of ultrathin monoclinic BiVO<sub>4</sub> nanosheets for Z-scheme overall water splitting under visible light, *ACS Catal.* 8 (2018) 8649–8658.
- [18] G. Wang, Y. Ling, X. Lu, F. Qian, Y. Tong, J. Zhang, V. Lordi, C. Leao, Y. Li, Computational and photoelectrochemical study of hydrogenated bismuth vanadate, *J. Phys. Chem. C* 117 (2013) 10957–10964.
- [19] Y. Liu, C. Xiao, Z. Li, Y. Xie, Vacancy engineering for tuning electron and phonon structures of two-dimensional materials, *Adv. Energy Mater.* 6 (2016), 1600436.
- [20] F. Xu, K. Meng, B. Cheng, S. Wang, J. Xu, J. Yu, Unique S-scheme heterojunctions in self-assembled TiO<sub>2</sub>/CsPbBr<sub>3</sub> hybrids for CO<sub>2</sub> photoreduction, *Nat. Commun.* 11 (2020) 4613.
- [21] X. Wang, J. He, J. Li, G. Lua, F. Dong, T. Majim, M. Zhu, Immobilizing perovskite CsPbBr<sub>3</sub> nanocrystals on Black phosphorus nanosheets for boosting charge separation and photocatalytic CO<sub>2</sub> reduction, *Appl. Catal. B: Environ.* 277 (2020), 119230.
- [22] J. Di, J. Xiong, H. Li, Z. Liu, Ultrathin 2D photocatalysts: Electronic-structure tailoring, hybridization, and applications, *Adv. Mater.* 30 (2018), 1704548.
- [23] X. Li, J. Yu, M. Jaroniec, Hierarchical photocatalysts, *Chem. Soc. Rev.* 45 (2016) 2603–2636.
- [24] S. Cao, B. Shen, T. Tong, J. Fu, J. Yu, 2D/2D heterojunction of ultrathin MXene/Bi<sub>2</sub>WO<sub>6</sub> nanosheets for improved photocatalytic CO<sub>2</sub> reduction, *Adv. Funct. Mater.* 28 (2018), 1800136.
- [25] Y. Sun, S. Gao, F. Lei, C. Xiao, Y. Xie, Ultrathin two-dimensional inorganic materials: new opportunities for solid state nanochemistry, *Acc. Chem. Res.* 48 (2015) 3–12.



- [26] Y. Jiang, H. Chen, J. Li, J. Liao, H. Zhang, X. Wang, D. Kuang, Z-Scheme 2D/2D heterojunction of CsPbBr<sub>3</sub>/Bi<sub>2</sub>WO<sub>6</sub> for improved photocatalytic CO<sub>2</sub> reduction, *Adv. Funct. Mater.* 30 (2020), 2004293.
- [27] J. Ran, W. Guo, H. Wang, B. Zhu, J. Yu, S. Qiao, Metal-Free 2D/2D phosphorene/g-C<sub>3</sub>N<sub>4</sub> van der Waals heterojunction for highly enhanced visible-light photocatalytic H<sub>2</sub> production, *Adv. Mater.* 30 (2018), 1800128.
- [28] B. Li, S. Liu, C. Lai, G. Zeng, M. Zhang, M. Zhou, D. Huang, L. Qin, X. Liu, Z. Li, N. An, F. Xu, H. Yi, Y. Zhang, L. Chen, Unravelling the interfacial charge migration pathway at atomic level in 2D/2D interfacial Schottky heterojunction for visible-light-driven molecular oxygen activation, *Appl. Catal. B: Environ.* 266 (2020), 118650.
- [29] H. Chuang, B. Chamlagain, M. Koehler, M. Perera, J. Yan, D. Mandrus, D. Tománek, Z. Zhou, Low-resistance 2D/2D ohmic contacts: A universal approach to high-performance WSe<sub>2</sub>, MoS<sub>2</sub>, and MoSe<sub>2</sub> transistors, *Nano Lett.* 16 (2016) 1896–1902.
- [30] L. Jiang, J. Duan, J. Zhu, S. Chen, Iron-cluster-directed synthesis of 2D/2D Fe-N-C/Mxene superlattice-like heterostructure with enhanced oxygen reduction electrocatalysis, *ACS Nano* 14 (2020) 2436–2444.
- [31] J. Su, G.D. Li, X.H. Li, J.S. Chen, 2D/2D heterojunctions for catalysis, *Adv. Sci.* 6 (2019), 1801702.
- [32] L. Protesescu, S. Yakunin, M. Bodnarchuk, F. Krieg, R. Caputo, C. Hendon, R. Yang, A. Walsh, M. Kovalenko, Nanocrystals of cesium lead halide perovskites (CsPbX<sub>3</sub>), X = Cl, Br, and I: Novel optoelectronic materials showing bright emission with wide color gamut, *Nano Lett.* 15 (2015) 3692–3696.
- [33] S. Sun, D. Yuan, Y. Xu, A. Wang, Z. Deng, Ligand-mediated synthesis of shape-controlled cesium lead halide perovskite nanocrystals via reprecipitation process at room temperature, *ACS Nano* 10 (2016) 3648–3657.
- [34] Y. Chen, H. Zeng, P. Ma, G. Chen, J. Jian, X. Sun, X. Li, H. Wang, W. Yin, Q. Jia, G. Zou, Overcoming the anisotropic growth limitations of free-standing single-crystal halide perovskite films, *Angew. Chem. Int. Ed.* 60 (2021) 2629–2636.
- [35] T. Sheng, N. Tian, Z.-Y. Zhou, W.-F. Lin, S.-G. Sun, Designing Pt-based electrocatalysts with high surface energy, *ACS Energy Lett.* 2 (2017) 1892–1900.
- [36] Q. Xiang, F. Li, D. Zhang, Y. Liao, H. Zhou, Plasma-based surface modification of g-C<sub>3</sub>N<sub>4</sub> nanosheets for highly efficient photocatalytic hydrogen evolution, *Appl. Surf. Sci.* 495 (2019), 143520.
- [37] X. Yue, X. Miao, Z. Ji, X. Shen, H. Zhou, L. Kong, G. Zhu, X. Li, S. Shah, Nitrogen-doped carbon dots modified dibismuth tetraoxide microrods: A direct Z-scheme photocatalyst with excellent visible-light photocatalytic performance, *J. Colloid Interf. Sci.* 531 (2018) 473–482.
- [38] J. Fu, Q. Xu, J. Low, C. Jiang, J. Yu, Ultrathin 2D/2D WO<sub>3</sub>/g-C<sub>3</sub>N<sub>4</sub> step-scheme H<sub>2</sub>-production photocatalyst, *Appl. Catal. B: Environ.* 243 (2019) 556–565.
- [39] X. Li, S. Lyu, X. Lang, Superoxide generated by blue light photocatalysis of g-C<sub>3</sub>N<sub>4</sub>/TiO<sub>2</sub> for selective conversion of amines, *Environ. Res.* 195 (2021), 110851.
- [40] J. Sheng, Y. He, J. Li, C. Yuan, H. Huang, S. Wang, Y. Sun, Z. Wang, F. Dong, Identification of halogen-associated active sites on bismuth-based perovskite quantum dots for efficient and selective CO<sub>2</sub>-to-CO photoreduction, *ACS Nano* 14 (2020) 13103–13114.
- [41] Z. Zhang, J. Huang, M. Zhang, Q. Yuan, B. Dong, Ultrathin hexagonal SnS<sub>2</sub> nanosheets coupled with g-C<sub>3</sub>N<sub>4</sub> nanosheets as 2D/2D heterojunction photocatalysts toward high photocatalytic activity, *Appl. Catal. B: Environ.* 163 (2015) 298–305.
- [42] Z. Kong, J. Liao, Y. Dong, Y. Xu, H. Chen, D. Kuang, C. Su, Core@Shell CsPbBr<sub>3</sub>@Zeolitic imidazolate framework nanocomposite for efficient photocatalytic CO<sub>2</sub> reduction, *ACS Energy Lett.* 3 (2018) 2656–2662.
- [43] J. Shamsi, Z. Dang, P. Bianchini, C. Canale, F. Stasio, R. Brescia, M. Prato, L. Manna, Colloidal synthesis of quantum confined single crystal CsPbBr<sub>3</sub> nanosheets with lateral size control up to the micrometer range, *J. Am. Chem. Soc.* 138 (2016) 7240–7243.
- [44] X. Ma, L. Wang, Q. Zhang, H.L. Jiang, Switching on the photocatalysis of metal-organic frameworks by engineering structural defects, *Angew. Chem. Int. Ed.* 58 (2019) 12175–12179.
- [45] X. Yang, S. Wang, N. Yang, W. Zhou, P. Wang, K. Jiang, S. Li, H. Song, X. Ding, H. Chen, J. Ye, Oxygen vacancies induced special CO<sub>2</sub> adsorption modes on Bi<sub>2</sub>MoO<sub>6</sub> for highly selective conversion to CH<sub>4</sub>, *Appl. Catal. B: Environ.* 259 (2019), 118088.
- [46] F. He, B. Zhu, B. Cheng, J. Yu, W. Ho, W. Macyk, 2D/2D/0D TiO<sub>2</sub>/C<sub>3</sub>N<sub>4</sub>/Ti<sub>3</sub>C<sub>2</sub> MXene composite S-scheme photocatalyst with enhanced CO<sub>2</sub> reduction activity, *Appl. Catal. B: Environ.* 272 (2020), 119006.
- [47] L. Cheng, H. Yin, C. Cai, J. Cai, Q. Xiang, Single Ni atoms anchored on porous few-layer g-C<sub>3</sub>N<sub>4</sub> for photocatalytic CO<sub>2</sub> reduction: The role of edge confinement, *Small* 16 (2020), e2002411.
- [48] Y. Li, M. Wen, Y. Wang, G. Tian, C. Wang, J. Zhao, Plasmonic hot electrons from oxygen vacancies for infrared light-driven catalytic CO<sub>2</sub> reduction on Bi<sub>2</sub>O<sub>3</sub>-x, *Angew. Chem. Int. Ed.* 60 (2021) 910–916.
- [49] X. Li, Y. Sun, J. Xu, Y. Shao, J. Wu, X. Xu, Y. Pan, H. Ju, J. Zhu, Y. Xie, Selective visible-light-driven photocatalytic CO<sub>2</sub> reduction to CH<sub>4</sub> mediated by atomically thin CuIn<sub>5</sub>S<sub>8</sub> layers, *Nat. Energy* 4 (2019) 690–699.